





Overview of the Precipitates in a Ground-Coat Vitreous Enamel Using Analytical TEM

S. Selle^{1,*}, H. Bornhöft², J. Wendel³, and J. Deubener²

¹ Fraunhofer Institute for Microstructure of Materials and Systems IMWS, 06120 Halle, Germany

² Clausthal University of Technology, Institute of Non-Metallic Materials, 38678 Clausthal-Zellerfeld, Germany

³ Wendel Email GmbH, 35683 Dillenburg, Germany

*Correspondence: Susanne Selle, susanne.selle@imws.fraunhofer.de

Abstract. Precipitates in the ground-coat vitreous enamel, which form when the dried coating is fired and cooled on sheet steel, are essential for the function of the enamelling. They lead to an interlocked metal-glass interface and are triggered by redox-driven processes in a glass layer saturated with iron. Using analytical transmission electron microscopy, it is shown that alloys of the Fe-Co-Ni-Cu system not only precipitate near the interface, where they contribute to adhesion through an interlocking interface, but also form nanocrystallites that are finely distributed in the enamelled glass to a depth determined by the diffusivity of Fe²⁺ (30 µm after four minutes of firing) and probably contribute to the toughening of this glass layer. The saturation with iron also prevents the segregation of the glass flux and opacifier calcium fluoride, which only occurs far from the interface in the chemically unmodified base glass. At the metal-glass interface, however, phosphorus traces diffuse from the steel and precipitates in the form of calcium phosphate needles that grow into the enamelled glass.

Keywords: Vitreous Enamel, Metal-Glass Interface, Precipitates, TEM, STEM-EDXS.

1. Introduction

Enamelling steel is an industrial practice that serves as an abrasion-, chemical- and corrosion-resistant coating [1] and enables a decorative design of the metal surface [2]. Due to the excellent durability of this type of coating and in view of the requirements of the circular economy with its careful use of energy and resources, vitreous enamelling is also attracting renewed interest as a sustainable coating process.

The mechanical and chemical properties, which are superior to those of paint and plastic powder coatings, are based on the reaction of the fritted glass particles with the steel surface at high temperatures. Already about 90 years ago, images of metallographic cross-sections (light microscopy with up to 1300-fold magnification [3]) showed the formation of a specific reaction layer, which has an irregular interface that contributes to the adherence of the fired enamel to steel sheet. Reviews of this pioneering work can be found in [4], [5], [6]. Over the years, details of this layer have been identified with the higher resolution of scanning electron microscopes (5000-fold magnification, firstly in 1958 [7]), which have now become the standard for material development in the enamel industry [8], [9], [10].

Based on the findings from optical and scanning electron microscopy, it is assumed that the reactions are initiated by the oxidation of iron (scale formation: magnetite (Fe₃O₄) [4]) during the initial phase of sintering, i.e. prior to the fusion of the ground-coat. With the formation

of a closed porosity and complete wetting in the final phase of sintering, the surface is cut off from direct oxygen supply, so that magnetite on the iron surface is reduced to FeO, which dissolves as Fe²⁺ in the vitreous enamel. With further oxygen diffusing in from the vitreous enamel, magnetite then precipitates in the glass above the saturation concentration of ferrous ions and forms an iron oxide layer at the metal interface. The saturation concentration in sodium borosilicate glasses is 40–43 wt% FeO [6], [11] or ~45 wt% Fe₂O₃ [12], which corresponds to approx. 9–15 at% Fe. It has been found that dissolution of this iron oxide layer is stimulated by so-called adherence promoters such as CoO and NiO [6], which are present in the ground-coat vitreous enamel as network-modifying Co²⁺, Ni²⁺ cations. In general, more iron can be oxidised to Fe²⁺ and dissolved in the glass by a redox reaction when metal cations with less negative oxidation potential than the base metal iron are reduced to their metallic form [6]. As a result of this redox reaction, precipitates of metallic Co-Ni-Fe alloys form near the interface and grow and bond with the base metal, forming an irregular interface (protrusions, dendrites) [13], [14], [15].

In the 1990s, a first transmission electron microscopy (TEM) study of the microstructure at the interface was carried out [16], which confirmed the above results but showed a high density of small (< 100 nm diameter) iron-rich intermetallic particles near the interface with the steel, also containing nickel, cobalt and titanium. It was suggested that these form when the enamel cools from the enamel temperature and that they play an important role in toughening the vitreous enamel in this region.

Analytical TEM was developed through the realisation and application of aberration correctors about 20 years ago. In particular, the scanning unit (scanning transmission electron microscopy STEM) in combination with high angle ring dark field (HAADF) and energy dispersive X-ray spectroscopy (EDXS) detectors for element selective imaging (element maps) enable the spatial assignment of crystal precipitates in glasses and their ensembles in high resolution. The present study is therefore motivated to reveal details of the precipitates that form at the steel-vitreous enamel interface in the light of the higher analytical power of these advanced electron microscopy techniques. In order to be as close as possible to industrial practice, a commercial, ready-to-use (RTU) ground-coat enamel as well as an enamellable (low carbon), cold-rolled sheet steel within regular thickness were used for this study.

2. Materials and Methods

2.1 Glass frits and steel substrate

In this study, a commercial ready-to-use (RTU) ground-coat enamel (Wendel Email GmbH, Dillenburg, Germany) containing a mixture of various ground glass frits and additives was used. According to the manufacturer, the RTU contains (wt%) 50–68 SiO₂, 3–10 B₂O₃, 2–3 Al₂O₃, 2–16 TiO₂, 1–12 CaO, 1 MgO, 2–3 Li₂O, 7–20 Na₂O, 1–5 K₂O with minor amounts of CaF₂, CoO, NiO and CuO. Cold rolled low carbon steel (DC04ED according to the standard EN 10027-1 (DIN EN 10209:2022-07 Beuth Verlag), Tata Steel, IJmuiden, The Netherlands) of composition (at%) 99.5 Fe, 0.0276 C, 0.0062 Si, 0.2454 Mn, 0.0102 P, 0.016 S, 0.0171 Cr, 0.0038 Mo, 0.0163 Ni, 0.0239 Al, 0.0079 Co, 0.0217 Cu, 0.0026 Nb, <0.001 Ti, 0.0266 V, 0.015 W, 0.0019 Sn, 0.0031 As, 0.0019 Zr, 0.0002 Ca, and 0.0078 B (arc/spark-OES, Spectro Analytical Instruments, Kleve, Germany) with 1.5 mm thickness was used as a substrate for enamelling. The steel surface was degreased with a commercial agent (Industrie Clean, Würth, Künzelsau, Germany) consisting of hydrocarbons (n-alkane, isoalkane, cycloalkane and n-hexane) and then rinsed with distilled cold water. A series of enamelled steel plates (10 × 10 cm²) were made by spraying 6 g of RTU slip onto the plates, resulting in a coating thickness of about 200 µm. The coated plates were dried at 80 °C for 0.5 hours and then fired at 800 °C in a preheated electric resistance furnace (Nabertherm, Lilienthal, Germany). After firing for 2, 3, 4 and 5 minutes, respectively, a plate was removed from the kiln and air-cooled. The temperature-time schedule to cover the relevant process window was based on previous work

[13]. Additional samples with extended firing times (7, 8 and 9 minutes) were produced to test the mechanical adherence.

2.2 Transmission electron microscopy

An analytical transmission electron microscope (Thermo Fisher FEI Titan3 G2 80-300, Hillsboro, Oregon, USA) with 300 kV accelerating voltage was used to study the microstructure at the metal-glass interface and to a depth of $\sim 40\ \mu\text{m}$ in the vitreous enamel. The scanning unit was used together with a HAADF detector of the same microscope to obtain STEM images. Contrast is partly dependent on the atomic number of the elements and therefore chemically sensitive. Element mappings were made in combination with an EDXS detector (Super-X, Thermo Fisher FEI, Hillsboro, Oregon, US). Spectra acquisition and further quantitative processing of the EDXS data was done using Esprit software (version 1.9, Bruker, Billerica, US).

Two different preparation methods were used to obtain electron-transparent TEM samples. If a site-specific sample is not required, wedge preparation is a comparatively simple and fast approach (see scheme Figure 1 B to D). Here, a mechanically thinned (e.g. by sawing and polishing) cross-sectional platelet is further thinned to electron transparency by low-energy Ar^+ ions. Thereby the upper part, i.e. the enamel layer, is partly thinned out to leave an electron transparent rim which goes down to the substrate. This technique yields large electron-transparent regions that are virtually artefact-free. To test the feasibility, a site-specific lift-out sample was also prepared by FIB (focused ion beam) processing, using an enamel chip obtained by hammering off the enamelled steel sheet (see schematic Figure 1 E to G). For better handling during FIB processing and for a smooth surface, the chip was glued to a blade and polished with Ar^+ ions.

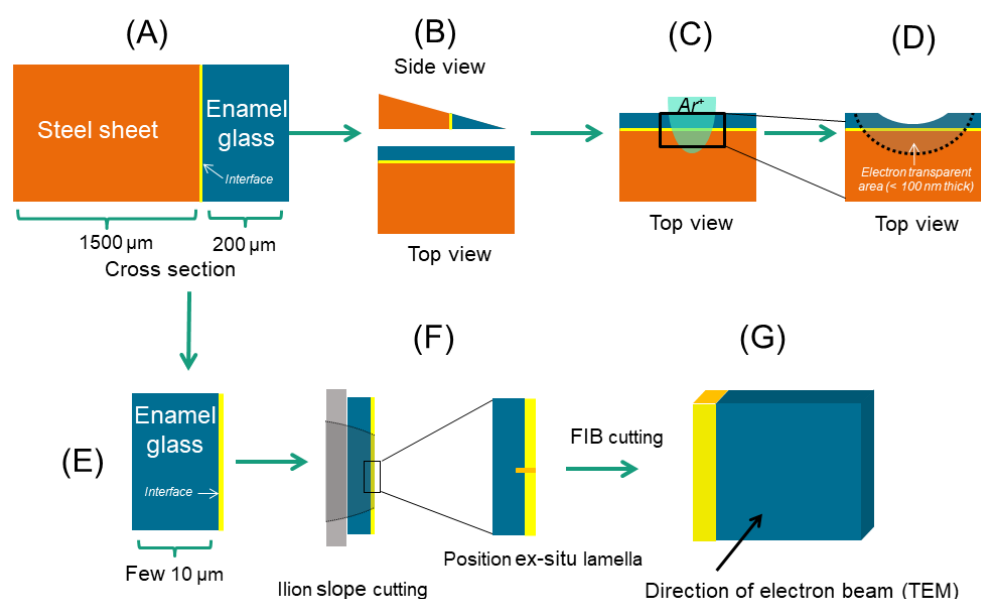


Figure 1. Preparation of electron transparent samples by (A–D) wedge grinding technique and (A, E–G) FIB machining. Note that the Ar^+ ion bombardment led to the complete removal of the glass in the center of the sample (D).

2.3 Electron probe microanalyses

To follow the iron diffusivity into the vitreous enamel, Fe line scans were carried out at different locations of the cross sections heated for 2 and 3 min (Figure 1A) using electron probe micro analyser (EPMA, SX100, Cameca, Gennevilliers Cedex, France). The instrument is equipped

with five wavelength dispersive spectrometers (WDS) and was operated at 15 kV, 20 nA, using a spot size of 16 μm along line scans.

2.4 Mechanical adherence tests

The adherence strength was performed with an accompanying cupping test, in which a cupping depth of 2.3 mm was sufficient to induce intensive chipping of the enamel with respect to the thickness of the steel substrate (1.5 mm). The damaged area after cupping was imaged using a digital microscope (Keyence VK-9710) to visualize the bare steel surface and remaining glass.

3. Results

3.1 Overview

Figure 2 shows an overview of the areas examined by TEM from the interface to a depth of about 40 μm in the vitreous enamel of the samples heated for 2, 3, 4 and 5 minutes. All images are TEM bright field (BF) except the STEM-HAADF images at the bottom of Figure 2, which show the microstructure directly at the interface. It is important to note that in the HAADF imaging technique the contrast is partly caused by the dependence on the atomic number Z , therefore materials composed of heavy elements appear bright and those consisting of light elements are dark. This is in contrast to the standard TEM-BF imaging where the unscattered (transmitted) electron beam is selected with the aperture and weak scattering areas appear bright while the strongly scattering precipitates appear dark.

At first glance, it is noticeable that precipitates occur over the entire depth examined. Here, a change from very small nanometric to larger round precipitates can be seen. This change occurs at a depth where the iron concentration drops from a relatively constant (saturation) level. In the initial glass of the RTU, iron is only present in traces that occur as contamination of the raw materials used and their processing. In the steel sheet, the iron content is almost 100%. The mean iron concentration as determined with EPMA on cross-sections of 2 and 3 min samples is shown in the form of a dash-dotted line as a cyan overlay on the TEM images. The change in the type of precipitates occurs at about 10–12 μm (2 min), 20–23 μm (3 min) and 26–31 μm (4 min). For the 2-minutes sample at 11 μm , the iron concentration was 2900 cps/18900 cps (iron sheet) \approx 15 at%, while for the 3-minutes sample at 21 μm 1900 cps/14700 cps (iron sheet) \approx 13 at% Fe was determined.

At the interface with the substrate (approx. to a depth of 3 μm), precipitation is more complex, which includes the formation of characteristic protrusions. This situation is first analysed in detail using STEM-EDXS element imaging, while precipitates further away from the interface are examined afterwards.

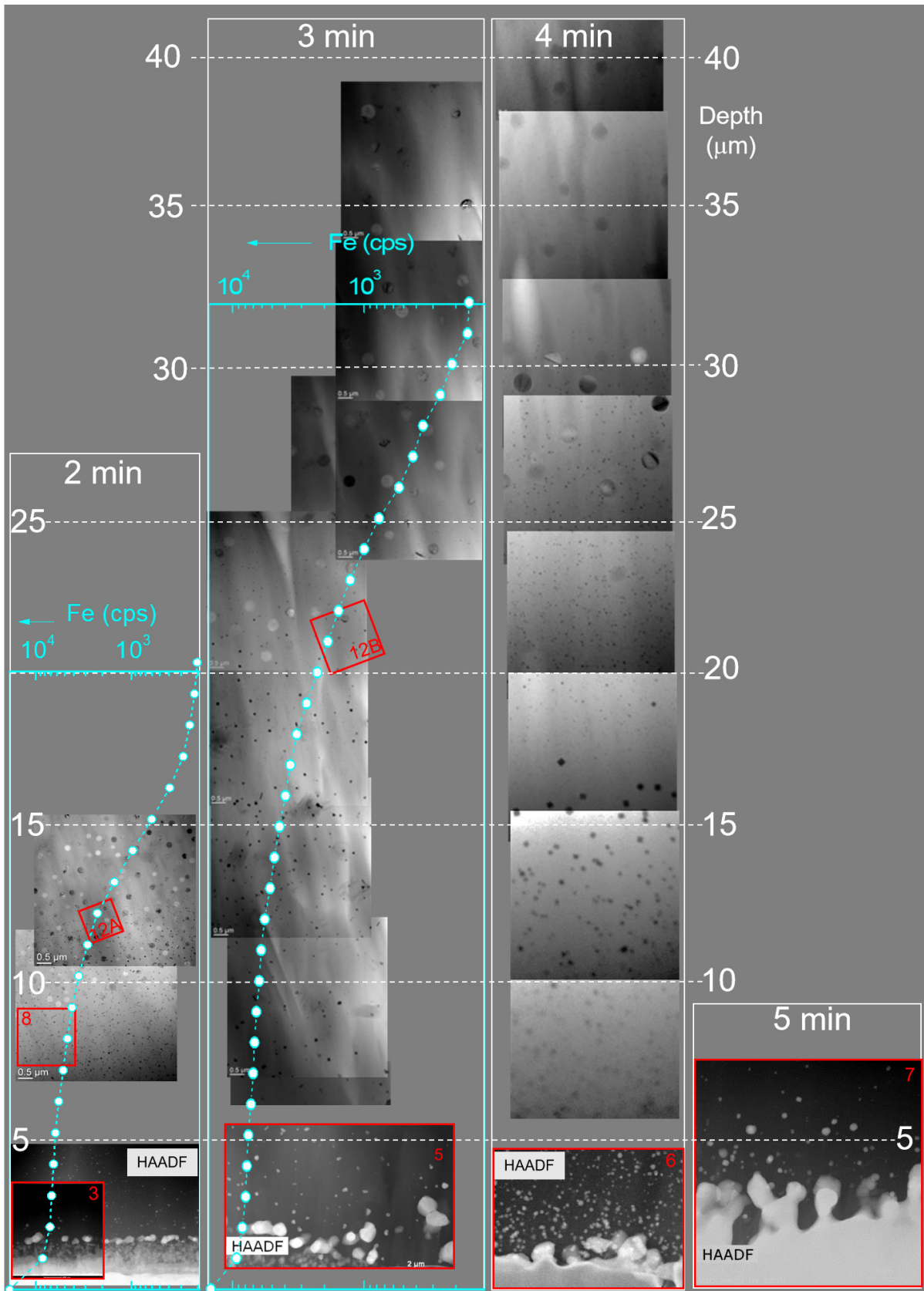


Figure 2. Overview of the areas studied with TEM near the interface and in the depth of the vitreous enamel. Bottom image of each sample is STEM-HAADF, while all other images are TEM-BF images. The cyan dash-dotted lines are EPMA scans of the iron concentration. The red squares show the corresponding areas of the STEM-EDXS element maps of the following numbered images.

3.2 Near interface precipitates

Figure 3 shows that after the two minutes holding time, the glass frit particles of the RTU enamel have sintered to form a continuous glass layer on the steel substrate, wetting it completely. The iron oxidation forms a layer (position 1) that appears somewhat darker in the mass contrast of the HAADF image than the unoxidised iron underneath, which can still be seen at the bottom edge of the image. The element maps of position 1 clearly show that this layer consists only of iron and oxygen. Based on the atomic ratio of areas A1 and A2 of Fe:O \approx 1:1.4 in the EDXS analysis, a mixture of magnetite (Fe_3O_4) and hematite (Fe_2O_3) was assigned to this layer. The hematite is then already formed by oxidation of magnetite.

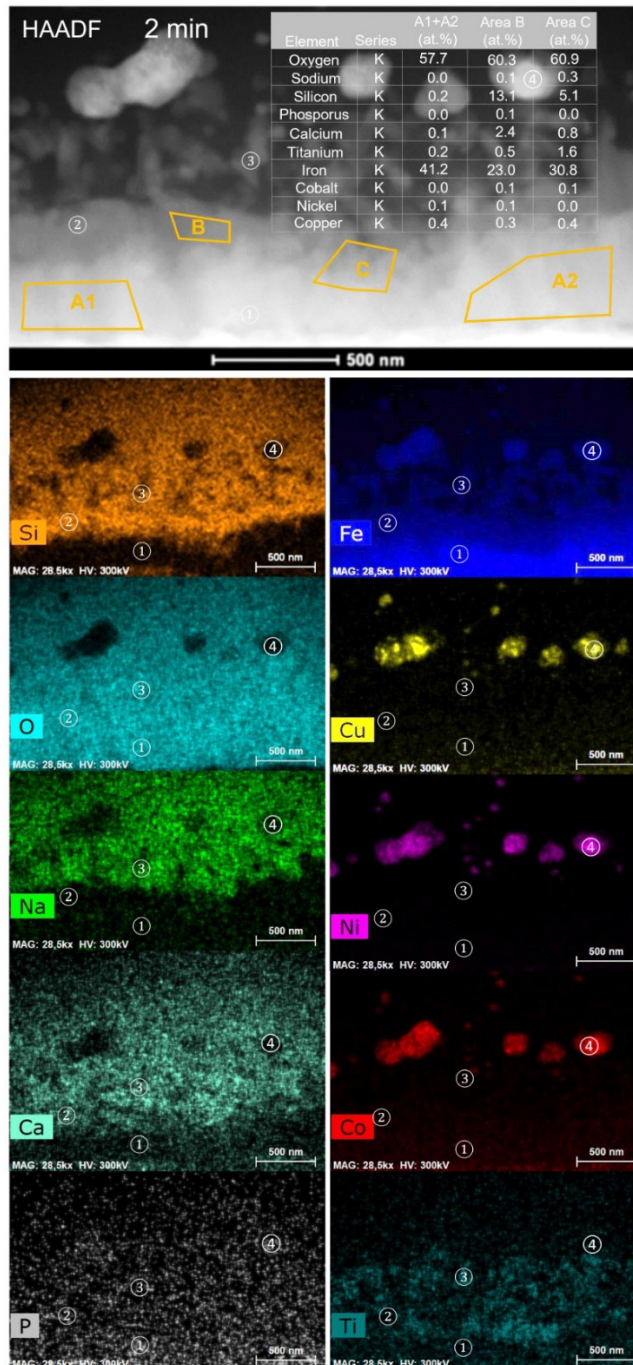


Figure 3. Near interface precipitates for heating RTU ground-coat on a steel substrate at 800 °C for 2 min with (1) magnetite/hematite, (2–3) fayalite and (4) Fe-Co-Ni-Cu alloy. STEM-HAADF image (bottom left) and STEM-EDXS element maps. Enlargement of the HAADF image (top) shows chemical composition (at%) of selected areas according to EDXS intensity. Scale bar is 500 nm in all sections.

Above the magnetite/hematite layer, another layer with even lower mass contrast is visible in the HAADF image (position 2). The element maps show that in addition to iron and oxygen, silicon is enriched in this layer. The EDXS atomic ratios of area B were Fe:O \approx 1:2.6 and Si:O \approx 1:4.6, indicating a layer rich in fayalite (FeSiO₄) crystallites (later confirmed by diffraction analysis). Thus, fayalite appears to be formed by the reaction of the iron oxides with the liquefied vitreous enamel as the mobility of network modifying Fe²⁺ in the glass above glass transition is much greater than that of the network forming Si⁴⁺. Fayalite crystallites have a large aspect ratio extending up to approx. 0.5 μ m into the vitreous enamel (position 3). The Ti elemental map shows an enrichment of titanium associated with the fayalite crystallites. However, the EDXS spectrum of area C (maximum in the turquoise Ti map) results in a Ti content of only 1.6 at.%, which would indicate a weak solubility of Ti in fayalite or the occurrence of a few very small ilmenite (FeTiO₃) crystallites that are co-precipitated. Crystallisation of fayalite on top of the magnetite/hematite layer was also confirmed by selected area diffraction (SED) (Figure 4).

Fayalite crystallites are capped by a striking globular precipitation (position 4 of Figure 3) that appears brightly in the HAADF. Unlike the others, the element maps show that this precipitate is oxygen-free and consists of the elements iron, cobalt, nickel and copper. It is therefore referred to as an alloy of these elements. In addition to the accumulation of these alloy crystallites at about 1.2 μ m depth, other small crystallites of this type are visible at greater depths in the enamelled glass.

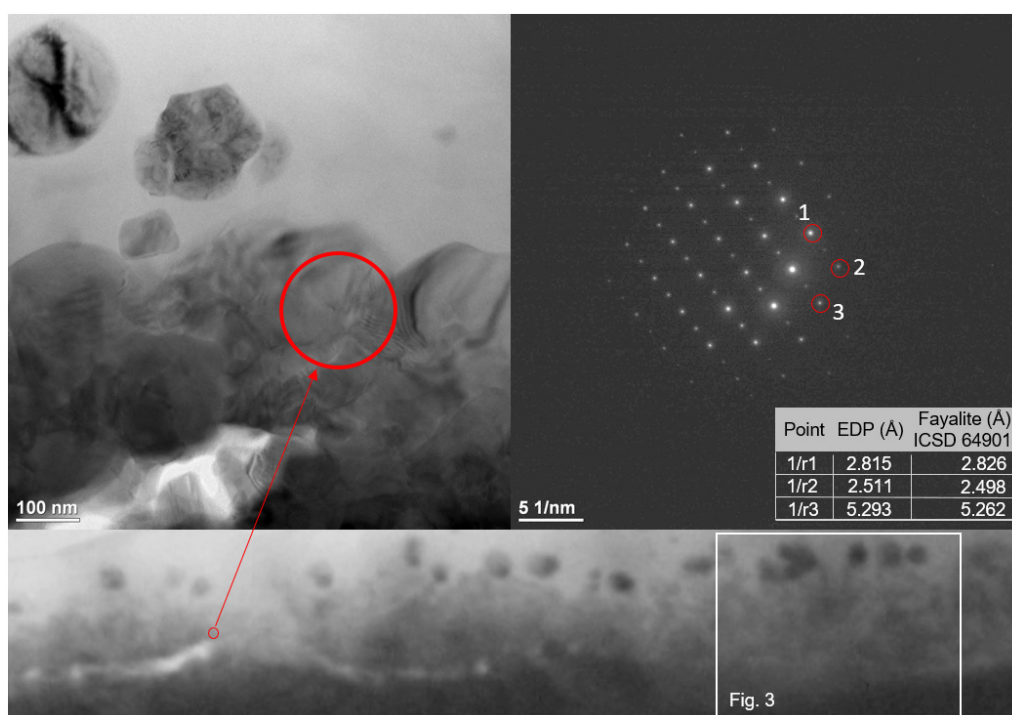


Figure 4. (Bottom) TEM-BF image of the near interface precipitates for heating RTU ground-coat on a steel substrate at 800 °C for 2 min in a larger section as Figure 3 with (top left) fayalite crystallites at higher magnification (projection of the SED aperture marked by the red circle) and (top right) pattern of received diffraction points matching fayalite (ICSD 64901) reference for the zone axis [-311].

After three minutes of tempering, the situation near the steel interface has already changed considerably (Figure 5). The intermediate fayalite crystallites seem to have dissolved in the vitreous enamel, while on position 1, remnants of crystallites containing Ti can still be seen. Since these crystallites also consist of oxygen and iron, but do not contain silicon, an assignment to ilmenite is being considered. The alloy precipitates (position 2), on the other hand, have grown considerably (note the difference in scale between Figure 3 and Figure 5). The Cu-Ni overlay image shows the spatial distributions of copper and nickel in these alloy

crystallites. It seems that larger crystallites are formed by smaller ones of different composition. Other nanometric crystallites of this type are finely distributed in the vitreous enamel. Position 3 shows the composition of the vitreous enamel, which is rich in calcium, sodium, silicon and oxygen. These elements are not detected in the precipitates with the exemption of oxygen in the Ti-bearing remnants.

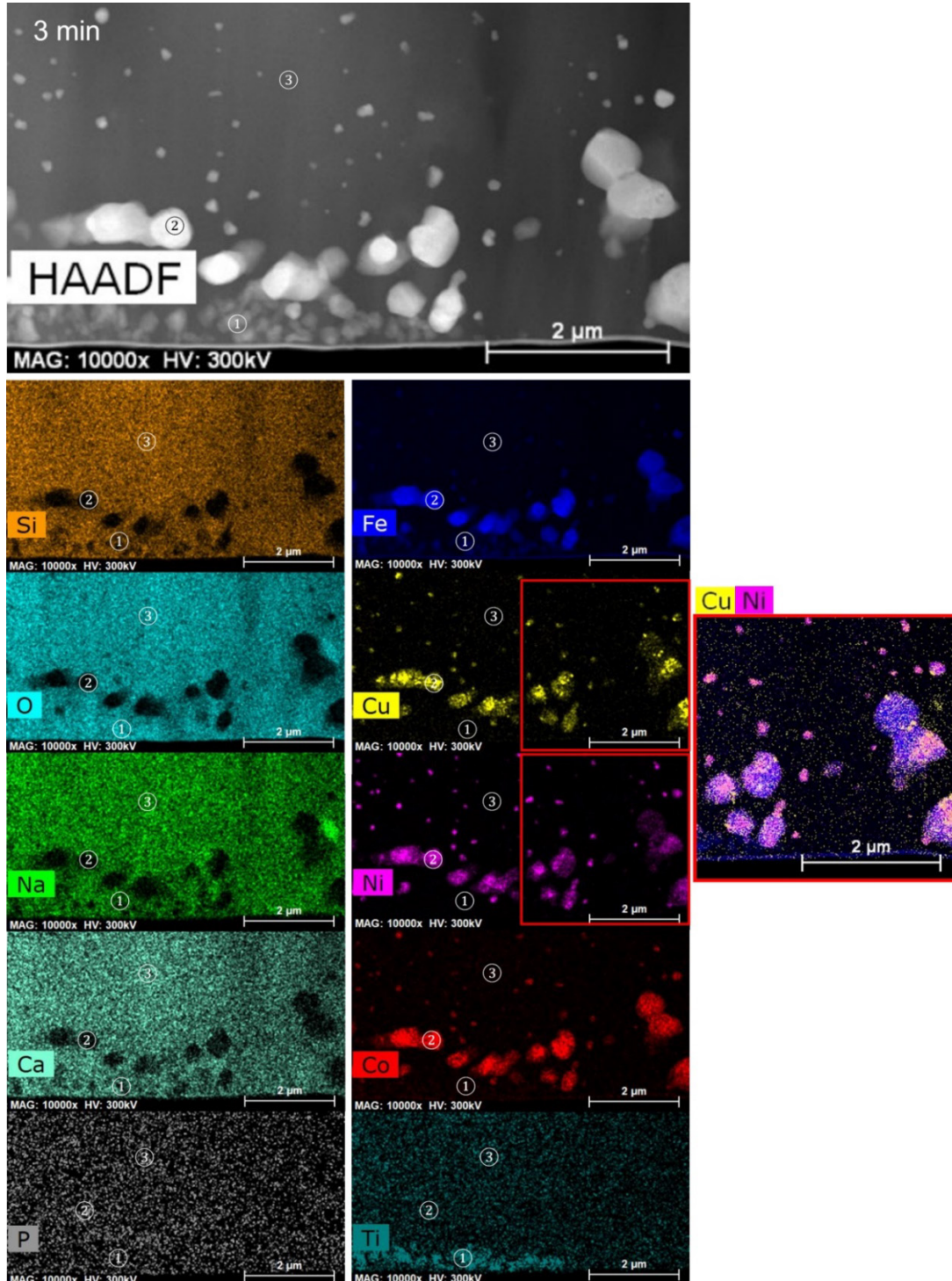


Figure 5. Near interface precipitates for heating RTU ground-coat on a steel substrate at 800 °C for 3 min with (1) ilmenite, (2) Fe-Co-Ni-Cu alloy and (3) vitreous enamel. STEM-HAADF image (top) and STEM-EDXS element maps. Cu-Ni overlay shows details (red square) of the copper-nickel distribution in the alloy crystallites (right row).

After four minutes, the steel-enamel interface already appears in the typical shape characterised by protrusions (Figure 6). It is thereby confirmed that these protrusions are formed by the growth of alloy precipitates on the steel. The element map of position 2 clearly shows the alloying elements Ni-Cu (overlay, left row of Figure 6), while the steel (position 1) is almost free of nickel and copper. In addition, a further precipitate is visible at position 3. Relatively large needles of calcium phosphate appear to have grown from the surface of the steel into the vitreous enamel, suggesting that phosphor from the steel combines with calcium ions from the vitreous enamel to form a nucleus at the solid-liquid interface. Even after four minutes of annealing, nanometric alloy crystallites are distributed in the vitreous enamel.

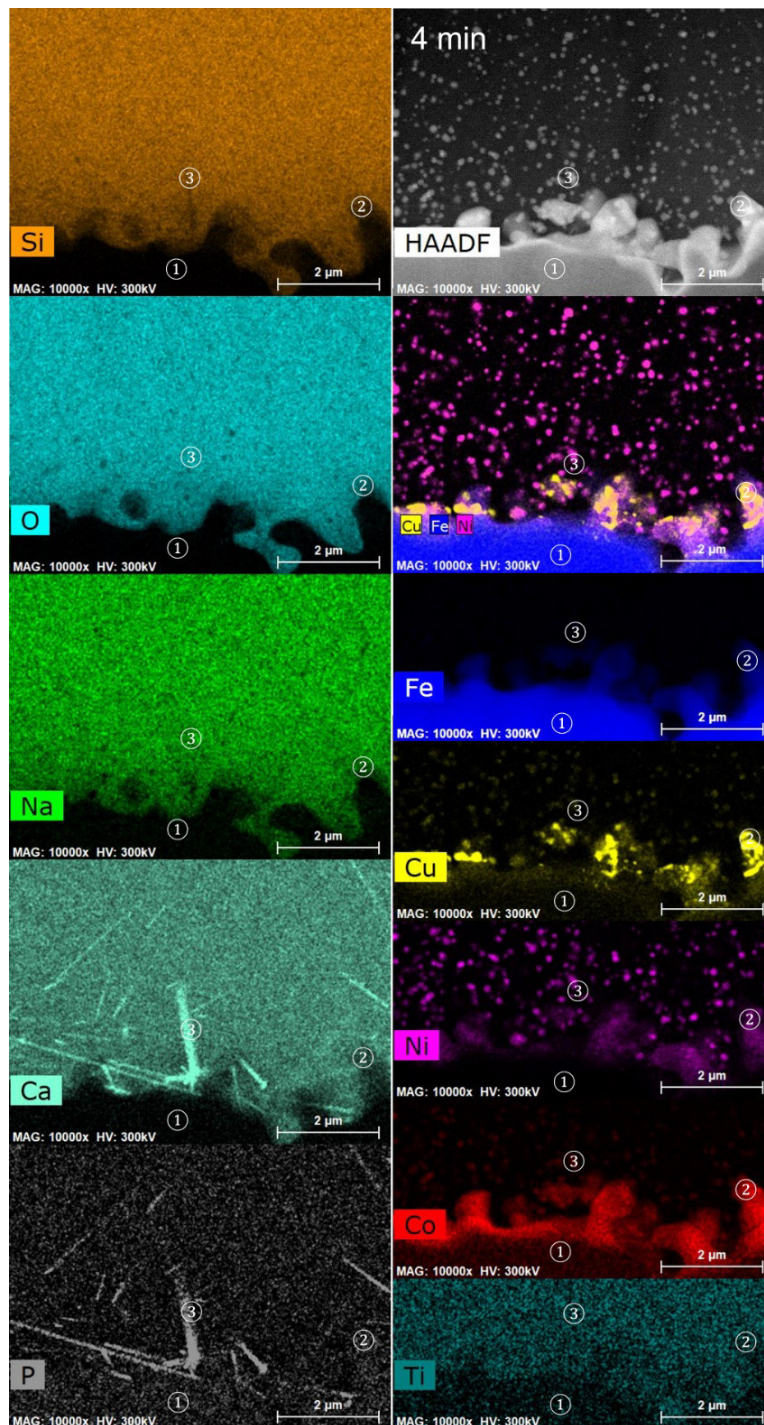


Figure 6. Near interface precipitates for heating RTU ground-coat on a steel substrate at 800 °C for 4 min with (1) steel, (2) Fe-Co-Ni-Cu alloy and (3) calcium phosphate. STEM-HAADF image (top right) and STEM-EDXS element maps.

Finally, after five minutes, the irregular shape of the metal-glass interface is fully formed (Figure 7). The protrusions show an enrichment of Ni, Cu and Co, which are alloying iron (position 1). Most strikingly, nano-alloys colonise the outer parts, which seems to be the mechanism of further growth (position 2). In addition, the calcium phosphate needles that have already grown after four minutes remain (position 3).

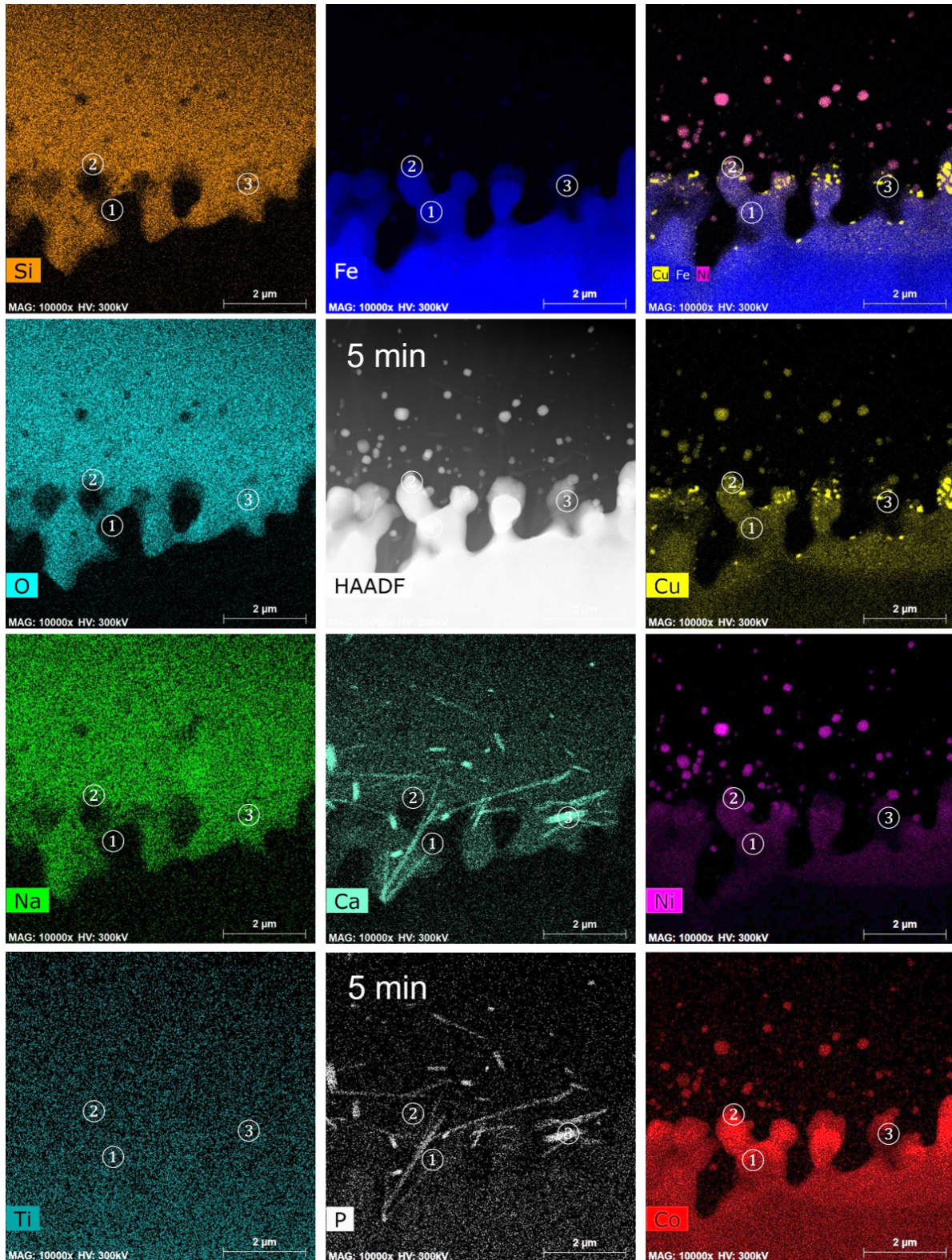


Figure 7. Near interface precipitates for heating RTU ground-coat on a steel substrate at 800 °C for 5 min with (1) Fe-Co-Ni-Cu protrusions, (2) colonising nano-alloys and (3) calcium phosphate needles.

3.3 Far interface precipitates

Figure 8 shows details of the nanometric crystallites at 8.5 μm depth (starting from the interface) of the vitreous enamel. Even at this depth, the elements form Fe-Co-Ni-Cu alloys. Their mixing ratios appear to become richer in nickel with increasing distance from the interface, as shown by the EDXS analysis compared to a crystallite situated at 3 μm depth. They are well-faceted cubes that have square or hexagonal shapes depending on their orientation to the electron beam, or they form elongated prisms (Figure 9). At higher magnification (magnified inset right part of Figure 8), details of the spatial distribution of Ni and Cu along the length of the crystal can be seen, indicating that, as in the alloy crystallites near the interface, growth occurs by coalescence of Cu and Ni rich particles.

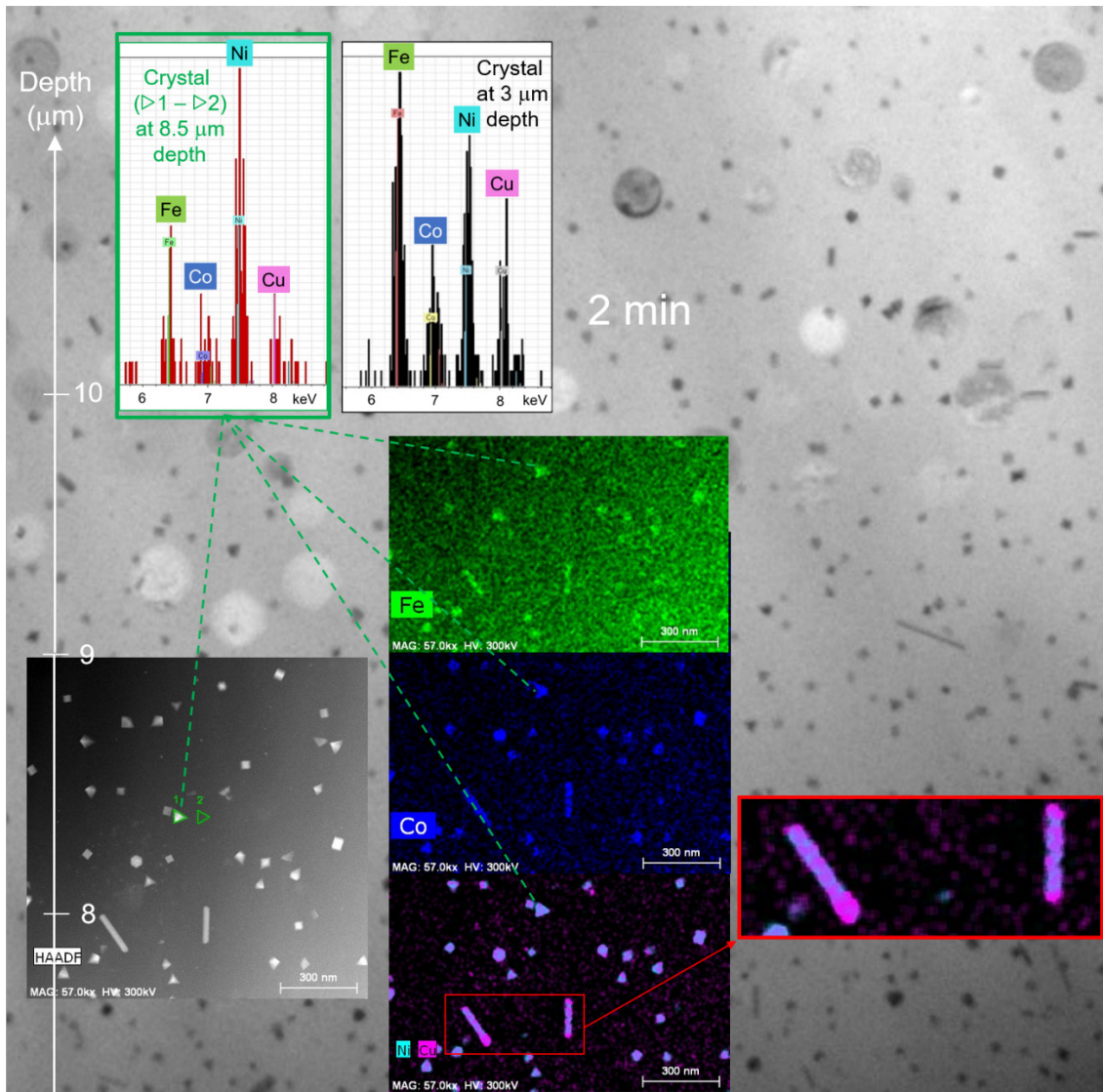


Figure 8. Details of Fe-Co-Ni-Cu alloy crystallites (STEM-HAADF overlaying TEM-BF image) at 8-9 μm depth from the steel-enamel interface of the 2-minutes sample. The centre shows STEM-EDXS element maps and top shows energy spectra of Fe, Co, Ni and Cu intensities of the marked crystal at 8.5 μm depth in comparison to another crystal at 3 μm depth. Right image shows Ni-Cu overlay of two elongated crystals at higher magnification.

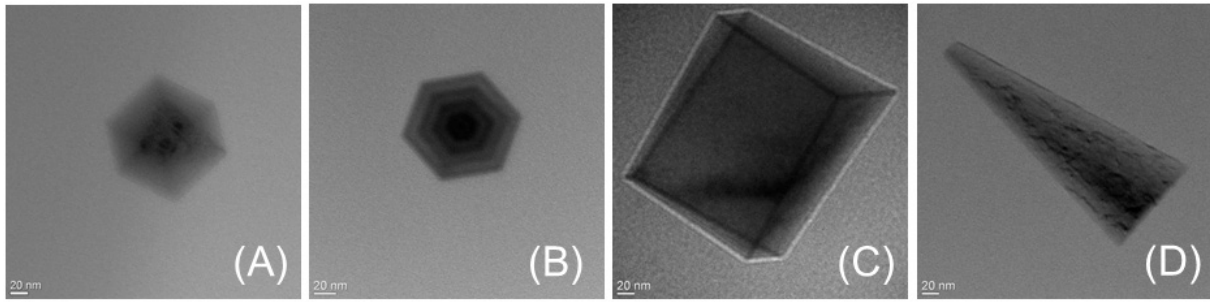


Figure 9. TEM-BF images of (A–B) cubic and (C–D) prismatic forms of Fe-Co-Ni-Cu alloy crystallites at $\sim 15 \mu\text{m}$ depth from the steel-enamel interface of the 3-minutes sample prepared by FIB machining. The images are partially defocused in order to increase the contrast at the edges of the particles. Note that the shapes of crystals shown are due to their electron transparency.

The analysis of the chemical composition by EDXS of a cubic crystallite (3-minutes sample, FIB cut) shows (Figure 10) that at $15 \mu\text{m}$ distance from the interface the ratio of nickel to the other alloying elements has further increased. Iron and cobalt are thus present only in traces, and the solid solution can be given the composition $\text{Fe}_{0.05}\text{Co}_{0.02}\text{Ni}_{0.69}\text{Cu}_{0.23}$, assuming that the counts of O, Si and Ca are artefacts resulting from the comparison of the spectra of sections 1 and 2.

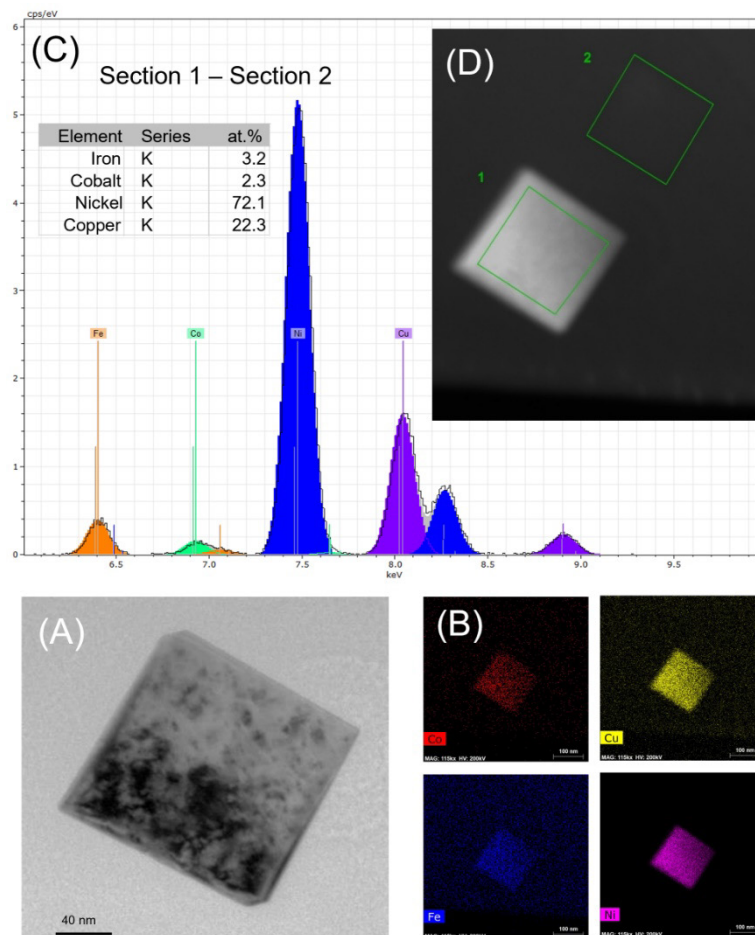


Figure 10. (A) Cubic Fe-Co-Ni-Cu alloy crystallite (TEM-BF image) at about $15 \mu\text{m}$ depth at the steel-enamel interface of the 3-minutes FIB cut sample. (B) STEM EDXS element maps and (C) EDX spectrum with normalised composition (D) determined by subtracting the EDX intensities of section 2 from those of section 1.

In order to investigate the alloy character also on a structural level, diffraction images of four crystallites were taken at different depths of the interface of the 5-minute sample (Figure 11). References for fcc Ni (ICSD 64989) and fcc Ni-Cu alloy, i.e. Ni, Ni_{0.08}Cu_{0.92} (ICSD 628545), Ni_{0.5}Cu_{0.5} (ICSD 628546) and Ni_{0.05}Cu_{0.95} (ICSD 628549) were used to analyse the diffraction patterns of Figure 11. It was found that the unit cell parameter *a* of the crystallites A and B far from the interface was shorter (354.5(5) pm) than for the crystallites C and D near the interface (357.7(5) pm), indicating an increasing substitution of large atoms by smaller ones with increasing depth and, with respect to the Ni/Cu ratio, an increase of smaller nickel atoms in the alloy crystallite with increasing depth.

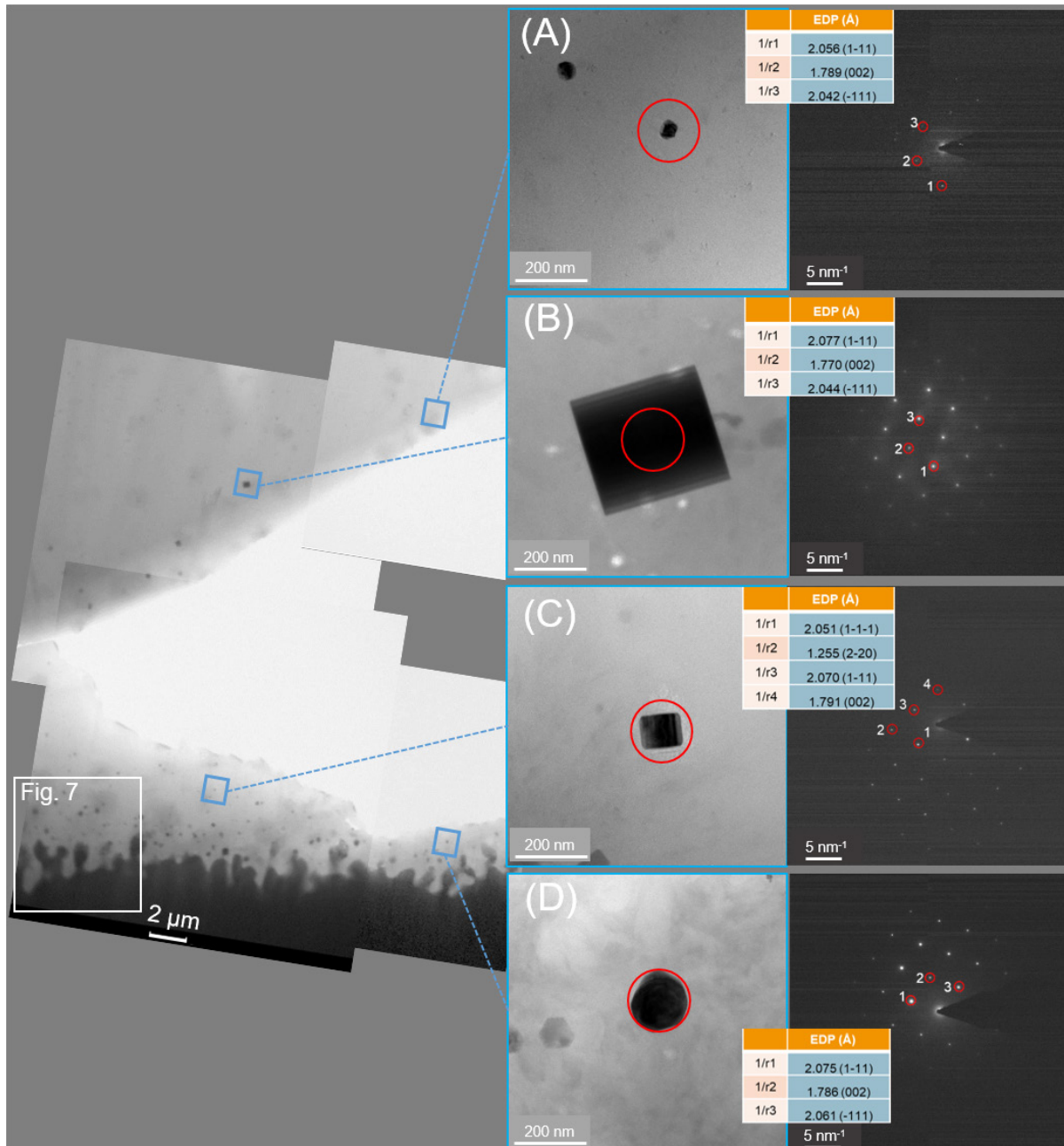


Figure 11. (Left) steel-enamel interface of the 5-minute sample in a larger section as Figure 7 with (centre column, from top to bottom) alloy crystallites at 22 μm (A), 18 μm (B), 3 μm (C) and 2 μm (D) depth at higher magnification (SED aperture in the red circle) and (right column) pattern of received diffraction points (zone axis [111]) matching cubic (fcc) Ni-Cu reference alloys.

At a greater distance from the steel interface, another type of precipitation occurs that has a spherical appearance. The EDXS element maps of the relevant elements of Figure 12 show

that this precipitation is as well non-oxidic and represents an enrichment of calcium and fluorine. They are therefore treated as droplets rich in calcium fluoride (CaF_2), which are the result of a liquid-liquid demixing process of the vitreous enamel during cooling. As can be seen in the overview (Figure 2), these segregation droplets only occur at a depth at which the iron concentration in the glass drops, i.e. approx. 10–12 μm (Figure 12, left) after two minutes and 20–23 μm after three minutes of firing. The precipitation of the alloy crystals ends in this depth range.

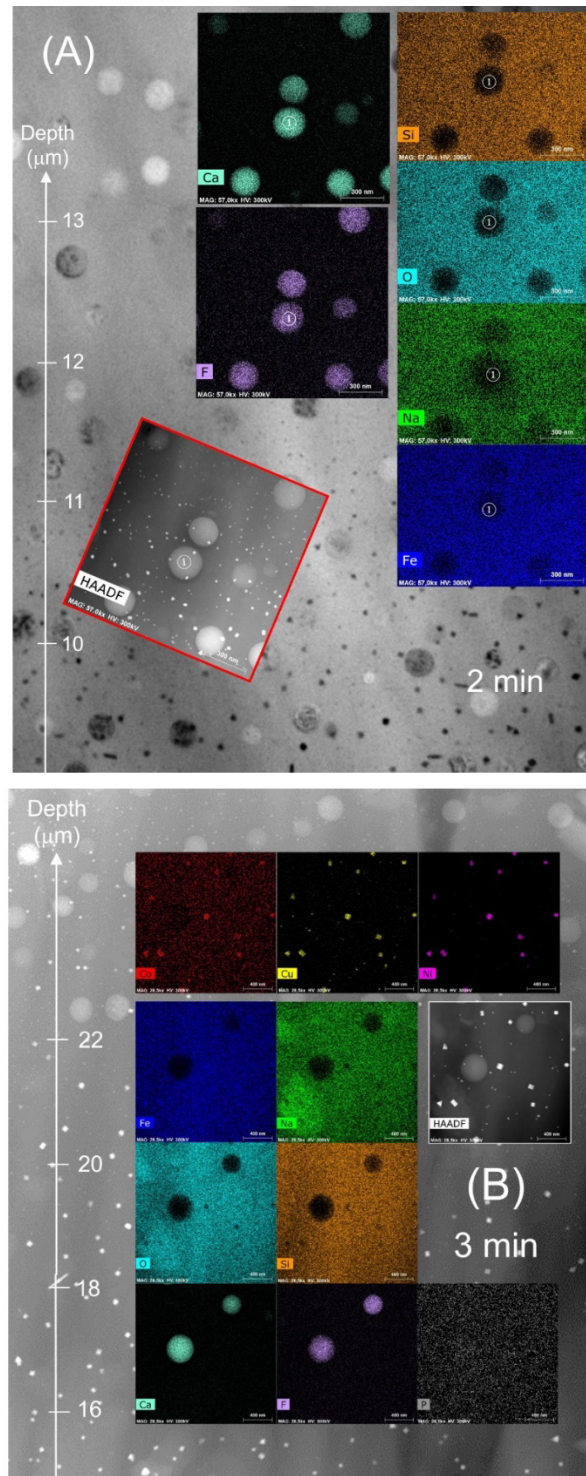


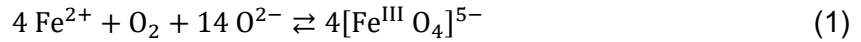
Figure 12. (A) Calcium fluoride-rich droplets at 11 μm (2 min sample) and (B) 21 μm (3 min sample) depth. (A) STEM-HAADF and STEM-EDXS element maps overlaying TEM-BF image. (B) STEM-EDXS element maps overlaying STEM-HAADF image.

4. Discussion

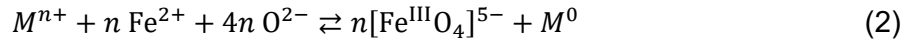
The results show that the reactions at the steel surface cause changes to a depth (about 31 μm after only 4 min) of the vitreous enamel that is larger than previously thought [16]. Thus, although a formal distinction can be made between the precipitates near the interface and those far from the interface, both are considered have an important role in the functionality of the enamel coating. Since this study does not cover the very early stages of enamel firing, which are associated with the scaling of the steel sheet and the sintering of the frit glass particles (a mechanically stable TEM sample could only be prepared after complete wetting of the coat), a surface covered with iron oxides (magnetite/hematite) is observed after a holding time of 2 min at 800 °C, which also leads to the crystallization of components of the liquid vitreous enamel. It can therefore be assumed that fayalite (Figure 4) and all other crystallites are precipitates from the liquid vitreous enamel caused by the initial dissolution of mobile iron species from the iron oxide layer, leading to a concentration up to saturation.

4.1 Fe-Co-Ni-Cu alloys

If mainly higher (six) coordinated Fe^{2+} contributes to the saturation iron concentration in the vitreous enamel shown in the EPMA line scans of Figure 2 (approx. 13–15 at%) then it can principally interact with both free oxygen anions (O^{2-}) of the glass and the O_2 partial pressure p_{O_2} leading to relative immobile ferric iron(III) that is tetrahedrally coordinated (network-forming) [17]:

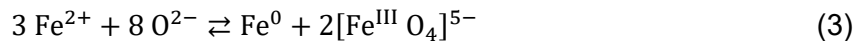


and with network modifying cations of nobler metals M^{n+} such as Cu^+ , Ni^{2+} and Co^{2+} of the glass (relatively mobile) that are capable of the redox reaction:



For the former interaction (Equation (1)), however, it should be noted that the oxygen partial pressure at the interface is very low after fusion of the enamelled glass. Thus, the concentration of ferrous cations (Fe^{2+}) is larger than that ferric cations (Fe^{3+}) in the network-forming complex $[\text{Fe}^{\text{III}} \text{O}_4]^{5-}$. To determine the conditions (oxygen partial pressure and $\text{Fe}^{2+}/\text{Fe}^{3+}$ ratio) under which metallic iron can precipitate in an enamelled glass, the results of Johnston [18] for a sodium disilicate melt consisting of 2 wt% iron were extended to 800 °C. For this purpose, the stability diagram (Ellingham diagram) was used to determine the partial pressure of oxygen that is in equilibrium with iron metal and ferrous oxide at a certain temperature ($2 \text{Fe} + \text{O}_2 = 2 \text{FeO}$). Figure 13 shows that for $\log p_{\text{O}_2} < -18.5$ and 800 °C, the $\text{Fe}^{2+}/\text{Fe}^{3+}$ ratio can be pushed above 0.9, i.e. $\log(\text{Fe}^{2+}/\text{Fe}^{3+}) > 1$, and metallic iron can be precipitated.

It was also found that under this condition, free oxygen anions (O^{2-}) in the glass, whose concentration is a measure of the glass basicity, favour the disproportionation of the ferrous oxide [18]:



For the latter interactions (Equations (2) and (3)), this means that the crystallisation of iron alloys still occurs to the depths of the saturation concentration of ferrous iron. For this, it is assumed that the alloy crystallisation is controlled by the diffusion rate of Fe^{2+} in the glass and that other processes involved in the formation, such as the electron transfer to form a neutral metal atom ($\text{Fe}^{2+} + 2 e^- \rightarrow \text{Fe}^0$ and $M^{n+} + n e^- \rightarrow M^0$ with e^- = electron) and the diffusion of iron and nobler metal atoms to form a nanometric iron alloy crystallite ($\text{Fe}^0 + xM^0 \rightarrow \text{Fe}_{(1-x)}M_x(\text{alloy})$) are fast [19].

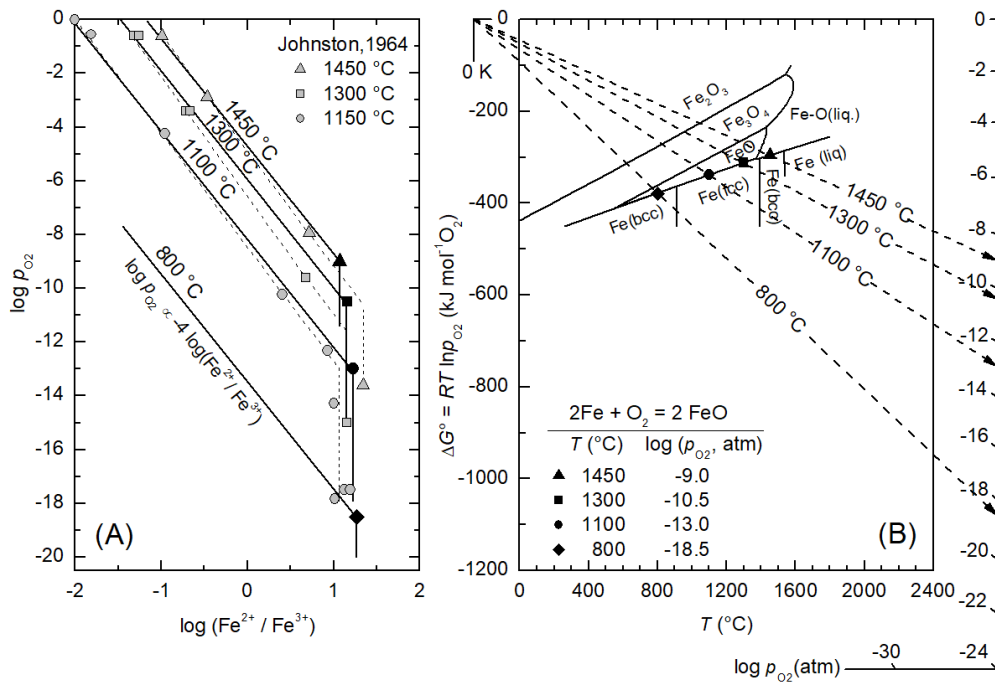
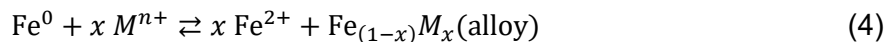


Figure 13. (A) Dependence of the $\text{Fe}^{2+}/\text{Fe}^{3+}$ ratio on the oxygen partial pressure p_{O_2} in sodium disilicate melts in logarithmic scales. The solid lines have a slope of -4 according to Equation (1), i.e. $\log p_{\text{O}_2}$ is proportional to -4 times $\log(\text{Fe}^{2+}/\text{Fe}^{3+})$. The $\text{Fe}^{2+}/\text{Fe}^{3+}$ ratio becomes independent of the oxygen partial pressure (vertical solid lines) when metallic iron precipitates at $\text{Fe}^{2+}/\text{Fe}^{3+} > 1$. Data and dashed lines are from Johnston [18] (B) Stability (Ellingham) diagram according to FactSage calculations from [20] and [21]. Determination of the p_{O_2} that is in equilibrium with metal iron and its ferrous oxide ($2\text{Fe} + \text{O}_2 = 2\text{FeO}$) at 800 °C and at 1450 °C, 1300 °C, 1100 °C to be consistent with the experimental data shown in part (A).

In contrast, Chen et al. [15] assumed the direct formation of iron alloys by the reduction of cations of nobler metals at the steel interface after dissolution of the oxide layer. Then one has [15]:



However, the details of the TEM analysis after a short firing time show (Figure 3) that alloy crystals are already precipitated while the oxide layer is still present on the steel surface, which makes direct reduction of Ni^{2+} , Co^{2+} and Cu^+ on the bare steel surface less likely in the initial phase. The presence of alloy crystallites that are not in direct contact with the steel interface is also shown for the later phases in the overview (Figure 2) and in detail in Figures 8, 9, 10 and 11.

In accordance with the stability of metal oxides at 800 °C ($\text{FeO} > \text{NiO} \approx \text{CoO} > \text{Cu}_2\text{O}$), one would assume that the effectiveness of the reducing agent (Fe^{2+}) increases with the difference in the free Gibbs energy of oxidation. The ease of reduction of nobler metal cations in terms of Equation (2) should therefore be in the order $\text{Cu}^+ > \text{Ni}^{2+} \approx \text{Co}^{2+}$. The required p_{O_2} or the required $\text{Fe}^{2+}/\text{Fe}^{3+}$ ratio is in turn much lower for the precipitation of copper metal than for nickel and cobalt metals. As the Fe^{2+} diffusion length increases over time in the depth of the enamelled glass, copper is precipitated earlier than nickel and cobalt during the enamelling process, preferably near the interface with the oxidised steel. Figures 8 and 10 show the ratios of these metals in the alloys of crystallites at depths of 3, 8.5 and 15 μm . It is clear that nickel is enriched in the crystallites far from the steel interface in relation to the other three metals (Fe, Co, Cu), while this excess is lower near the interface and the relative cobalt content is highest for the crystallites at 3 μm . Another point is that the high-resolution images in Figure 8 show a spatial chemical heterogeneity of the nanocrystallites, indicating a possible growth by coalescence of smaller Ni- and Co-rich crystallites. In the light of the above, this means that the average

composition depends on the number density of the primary Co-, Ni- and Cu-rich crystallites, which is then relatively high for copper near the interface and vice versa higher for nickel far from the interface.

These finely dispersed metallic precipitates mean that the glass must be considered more as a metal-nanocluster glass composite (MNCG), where the metallic phase makes an independent contribution to the properties of the composite. MNCGs are known to have optical, electrical and magnetic properties that make them promising candidates for a variety of optical and electronic applications, e.g. optical switches, magnetic recording media and new display materials [22]. However, in terms of enamelling, the mechanical properties of MNCGs need to be accounted for, as it was recently shown that copper-metal nanoparticles implanted into the bottom layer of commercial soda-lime silica glass lead to higher toughness [23]. The experimentally observed phenomena of intrinsic toughness increase were explained in particular by the fact that crack propagation within the layer implanted with metal nanoparticles comes to a standstill due to stress dissipation or relaxation. Recent work using electron microscopy has shown that despite their low volume fraction (0.5 vol. %), the dispersion of metallic Ni nanoparticles increases the fracture toughness of glass through dissipation mechanisms such as crack bridging [24]. In this context, these mechanisms could also contribute to the adhesive strength of the enamelled glass, as early electron microscopic studies have already suggested [16]. A further indication results from the accompanying cupping tests. While the enamelled glass does not adhere to the steel before the formation of the protrusions at the boundary layer (see Figures 2 and 5) and flakes off completely (2-4 min), cracks occur at longer firing times (5-7 min) in the unreacted glass, i.e. the entire iron-saturated MNCG layer (depth up to $\sim 75 \mu\text{m}$ after 7 min) increasingly remains on the steel after cupping, as Figure 14 shows.

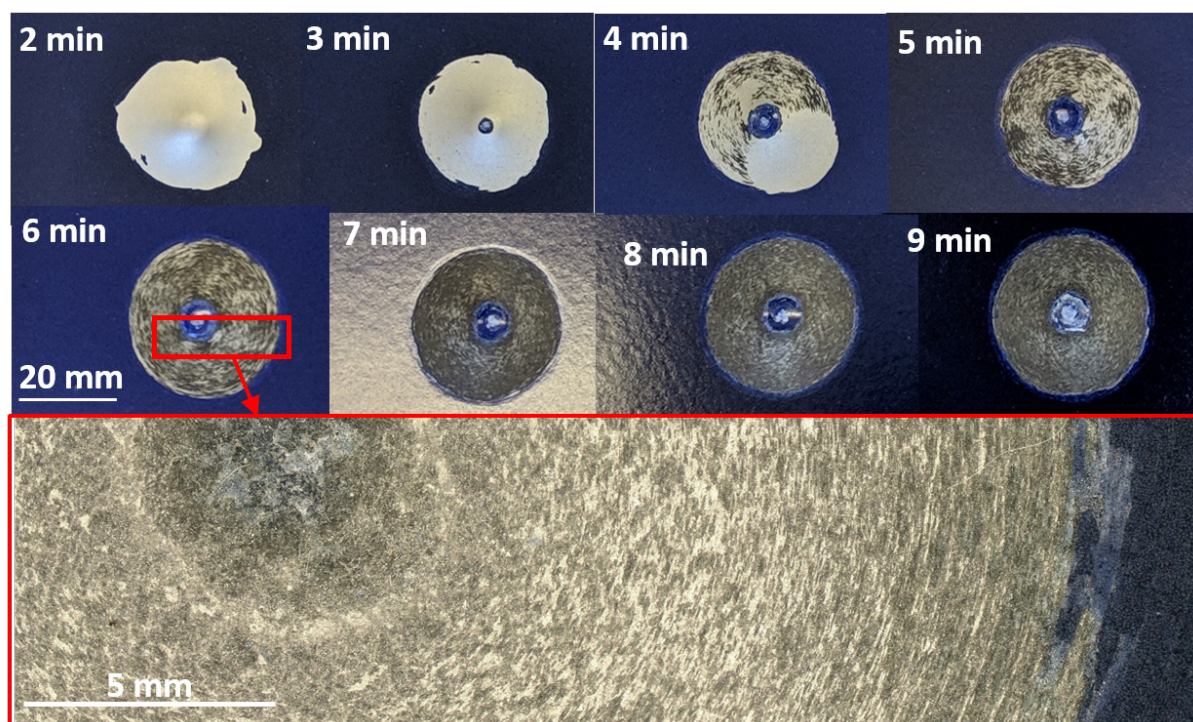


Figure 14. Visual appearance of the cupped area after 2-9 min firing time. Insufficient adherence: bare steel surface, i.e. the enamel has completely flaked off (2-4 min). Good adherence: dark MNCG layer remains on the steel sheet, i.e. cracking occurs in the unaltered glass (5-9 min).

4.2 Calciumphosphate

The occurrence of calcium phosphate needles only at firing times ≥ 4 min indicates that the enamelled glass is also enriched with phosphorus from the steel during firing (see Figures 6

and 7). As phosphorus is dissolved in the glass in the form of pentavalent, network-forming cations, their mobility is relatively low and only leads to a build-up near the glass-steel interface. As soon as a certain supersaturation is reached, crystallisation appears to start on cooling by heterogeneous nucleation at the steel surface. Calcium phosphate is known for its relatively high growth rates even at deep undercooling close to the glass transition temperature [25], and noble metal surfaces are also reported to promote heterogeneous nucleation of calcium phosphate crystals [26]. It can therefore be assumed that the relative high Cu content of the alloy precipitates near the interface (see Figure 6) also plays a possible role in the heterogeneous crystal nucleation of calcium phosphate.

4.3 Calciumfluoride

Calciumfluoride is known as a strong fluxing agent to steelmaking slags of high basicity as it reduces the liquidus temperature and the viscosity of the slags. When fluoride is added, the electrostatic bonds between NBO and Ca^{2+} are broken, resulting in $(\text{CaF})^+$ ion pairs that are weaker bound to the silicate anions and thus reduce the flow resistance [27]. This structural role also appears to be present in the case of the Fe^{2+} -saturated glass layer. However, if the basicity is reduced by a higher content of B_2O_3 and SiO_2 in the base glass, a calcium fluoride-rich glass tends to demix from the borosilicate matrix during cooling [28], [29]. In addition to the flux effect, calcium fluoride is an opacifier, as the differences in refractive index between fluoride and borosilicate glass lead to diffuse light scattering at the droplet interfaces. Interestingly, this function is inhibited by the increased basicity of the Fe-rich glass layer.

5. Conclusions

The results of this TEM analysis show that the enamelling leads to much more far-reaching influences in the enamelled glass than previously assumed. Particularly striking is the precipitation of alloy crystallites on the nanoscale, which is associated with the saturation of divalent iron cations in glass and which spreads diffusively to a relatively great depth of approximately 30 μm after four minutes of firing. Following the ease of reduction to metal, the alloy crystallites are richer in Cu and Co near the interface with the steel and become richer in Ni with greater distance from the steel-enamelled glass interface. As a result, this layer appears as a metal nanocluster composite glass in which the metal phase could add fracture toughness-promoting mechanical properties and thus not only the interlocking of the interface to the steel sheet would contribute to the mechanical adhesion of the enamelling.

Data availability statement

Data will be made available on request.

Author contributions

S. Selle: Funding acquisition, Investigation, Methodology, Validation, Writing – review & editing. H. Bornhöft: Investigation, Methodology, Validation, Writing – review & editing. J. Wendel: Resources, Validation, Writing – review & editing. J. Deubener: Conceptualization, Funding acquisition, Visualization, Writing – original draft, Writing – review & editing.

Competing interests

The authors declare that they have no competing interests.

Funding

J.D. and S.S. thanks the Deutsche Forschungsgemeinschaft (DFG) for providing funding under grant DE 598/30-1 and SE 2796/2-1, respectively.

References

- [1] S. Rossi, F. Russo, and M. Calovi, “Durability of vitreous enamel coatings and their resistance to abrasion, chemicals, and corrosion: a review”, *J. Coat. Technol. Res.* vol. 18, pp. 39–52, 2021, doi: <https://doi.org/10.1007/s11998-020-00415-3>.
- [2] S. Hoskins and E. Turrell, “Digital print technologies and their relation to vitreous enamel on metal for the visual artist”, in: *NIP & Digital Fabrication Conf., Soc. Imaging Sci. Technol.*, 2006, pp. 316–320.
- [3] H. Schaarschuh, “Ueber die Haftung von Blechgrundemails“, *Glashütte*, vol. 63, pp. 811–819, 1933.
- [4] A. Dietzel and K. Meures, *Sprechsaal*, vol. 66, pp. 647–652, 1933.
- [5] K. Kautz, “Further data on enamel adherence”, *J. Am. Ceram. Soc.*, vol. 47, pp. 198–201, 1936, doi: <https://doi.org/10.1111/j.1151-2916.1936.tb19804.x>.
- [6] B. W. King, H.P. Tripp, and W. H. Duckworth, “Nature of adherence of porcelain enamels to metals”, *J. Am. Ceram. Soc.*, vol. 42, pp. 504–525, 1959, doi: <https://doi.org/10.1111/j.1151-2916.1959.tb13567.x>.
- [7] J. Berk and J. de Jong, “On the adherence of porcelain enamel to sheet steel”, *J. Am. Ceram. Soc.*, vol. 41, pp. 287–293, 1958, doi: <https://doi.org/10.1111/j.1151-2916.1958.tb12918.x>.
- [8] A. Zucchelli, M. Dignatici, M. Montorsi, R. Carlotti, C. Siligardi, “Characterization of vitreous enamel–steel interface by using hot stage ESEM and nano-indentation techniques”, *J. Europ. Ceram. Soc.*, vol. 32, pp. 2243–2251, 2012, doi: <https://doi.org/10.1016/j.jeurceramsoc.2012.03.008>.
- [9] S. Rossi, F. Russo, V. Fontanari, and A. Compagnoni, “Innovative enamel coatings with improved mechanical properties by graphene and stainless steel addition”, *Procs. 25th Int. Enamellers Congress, International Enamellers Institute (IEI), Japan Enamel Association (JEA) and Tomatec Co. Ltd. (Japan), Kyoto, 2023*, pp. 1–7.
- [10] S. Pieters, C. Myers, and K. Lips, “A new horizon direct-on light colours”, *Procs. 25th Int. Enamellers Congress, International Enamellers Institute (IEI), Japan Enamel Association (JEA) and Tomatec Co. Ltd. (Japan), Kyoto, 2023*, pp. 1–7.
- [11] A. H. Dietzel, “Emaillierung – Wissenschaftliche Grundlagen und Grundzüge der Technologie”, Springer-Verlag, Berlin, 1981, pp.119–128, ISBN 3-540-10453-4.
- [12] M. M. Eltabey H. A. Othman, S. E. Ibrahim, L. M. Sharaf El-Deen, and M. M. Elkholy, “Structural, electrical and magnetic properties of high iron content sodium borosilicate glass”, *IOSR J. Appl. Phys.*, vol. 8, pp. 95–102, 2016, doi: <https://doi.org/10.9790/4861-08020195102>.
- [13] S. Striepe, H. Bornhöft, J. Deubener, and J. Wendel, “Fe-Co-Ni-Cu-microalloy precipitation enabling enamel adherence”, *J. Appl. Ceram. Technol.*, vol. 13, pp. 191–199, 2016, doi: <https://doi.org/10.1111/ijac.12435>.
- [14] J. Cha, J. Shin, J. Bae, D. Jeong, and B. Ryu, “Compositional dependence of structure and wetting properties of CoO-doped silicate glass for porcelain enamel”, *J. Ceram. Soc. Japan*, vol. 126, pp. 469–474, 2018, doi: <http://doi.org/10.2109/jcersj2.18026>.
- [15] K. Chen, M. Chen, Q. Wang, S. Zhu, and F. Wang, “Micro-alloys precipitation in NiO- and CoO-bearing enamel coatings and their effect on adherence of enamel/steel”, *Int. J. Appl. Glass Sci.*, vol. 9, pp. 70–84, 2018, doi: <https://doi.org/10.1111/ijag.12284>.
- [16] W. J. Nisbet, G. W. Lorimer, C. Sherhod, and M. J. Stowell, “Dual phase vitreous enamels, part 3 – Transmission electron microscopy of enamel / substrate interface”, *Mater. Sci. Technol.*, vol. 6, pp. 182–185, 1990, doi: <https://doi.org/10.1179/mst.1990.6.2.182>.

- [17] H. Scholze, "Glas – Natur, Struktur und Eigenschaften", Springer-Verlag, 3. Aufl., pp. 217–222, 1988, ISBN 3-540-18977-7.
- [18] W. D. Johnston, "Oxidation-reduction equilibria in iron-containing glass", *J. Am. Ceram. Soc.*, vol. 19, pp. 93–108, 1964, doi: <https://doi.org/10.1111/j.1151-2916.1964.tb14392.x>.
- [19] L.C. Briese, S. Selle, C. Patzig, Y. Hu, J. Deubener, and T. Höche, "Compositional study on the size distribution of nickel nanocrystals in borosilicate glasses", *J. Non-Cryst. Solids*, vol. 549, art. no. 120357, 2020, doi: <https://doi.org/10.1016/j.jnoncrysol.2020.120357>.
- [20] D. Klimm and S. Ganschow, "The control of iron oxidation state during FeO and olivine crystal growth", *J. Cryst. Growth*, vol. 275, pp. e849–e854, 2005, doi: <https://doi.org/10.1016/j.jcrysgro.2004.11.080>.
- [21] D. Channei, S. Phanichphant, A. Nakaruk, S. M. Sajjad, P. Koshy and C. C. Sorrell, "Aqueous and surface chemistries of photocatalytic Fe-doped CeO₂ nanoparticles", *Catal.*, vol. 7, art. no. 45, 2017, doi: <https://doi.org/10.3390/catal7020045>.
- [22] F. Gonella and P. Mazzoldi, "Chapter 2 – Metal nanocluster composite glasses", in: *Handbook of nanostructured materials and nanotechnology* (ed. H.S. Nalwa), vol. 4, pp. 81–158, 2000, doi: <https://doi.org/10.1016/B978-012513760-7/50044-7>.
- [23] M. Ono, S. Miyasaka, Y. Takato, S. Urata, H. Yoshino, R. Ando, and Y. Hayashi, "Higher toughness of metalnanoparticle-implanted sodalime silicate glass with increased ductility", *Sci. Rep.*, vol. 9, art.-no. 15387, 2019, doi: <https://doi.org/10.1038/s41598-019-51733-5>.
- [24] L. Liu and K. Shinozaki, "Brittle–ductile transition and toughening of silica glass via Ni nanoparticle incorporation at a small volume fraction", *J. All. Comp.*, vol. 940, art. no. 168874, 2023, doi: <https://doi.org/10.1016/j.jallcom.2023.168874>.
- [25] Y. Abe, T. Arahori, and A. Naruse, "Crystallization of Ca(PO₃)₂ glass below the glass transition temperature", *J. Am. Ceram. Soc.*, vol. 59, pp. 487–490, 1976, doi: <https://doi.org/10.1111/j.1151-2916.1976.tb09414.x>.
- [26] V. Guencheva, E. Stoyanov, I. Gutzow, C. Günter, and C. Rüssel, "Induced crystallization of glass-forming melts: Part 1. Heterogeneous nucleation. Effect of noble metal microcrystals on the crystallization of calcium metaphosphate glasses", *Glass Sci. Technol.*, vol. 77, pp. 217–228, 2004, doi: <https://doi.org/10.34657/12949>.
- [27] Y. Miyabayashi, M. Nakamoto, T. Tanaka and T. Yamamoto, "Model for estimating the viscosity of molten aluminosilicate containing calcium fluoride", *ISIJ Int.*, vol. 49, pp. 343–348, 2009, doi: <https://doi.org/10.2355/isijinternational.49.343>.
- [28] W. Vogel, "Phase separation in glass", *J. Non.-Cryst. Solids*, vol. 25, pp. 170–214, 1977, doi: [https://doi.org/10.1016/0022-3093\(77\)90093-X](https://doi.org/10.1016/0022-3093(77)90093-X).
- [29] I. V. Veksler, A. M. Dorfman, P. Dulski, V. S. Kamenetsky, L. V. Danyushevsky, T. Jeffries and D. B. Dingwell, "Partitioning of elements between silicate melt and immiscible fluoride, chloride, carbonate, phosphate and sulfate melts, with implications to the origin of natrocarbonatite", *Geochim. Cosmochim. Acta*, vol. 79, pp. 20–40, 2012, doi: <https://doi.org/10.1016/j.gca.2011.11.035>.